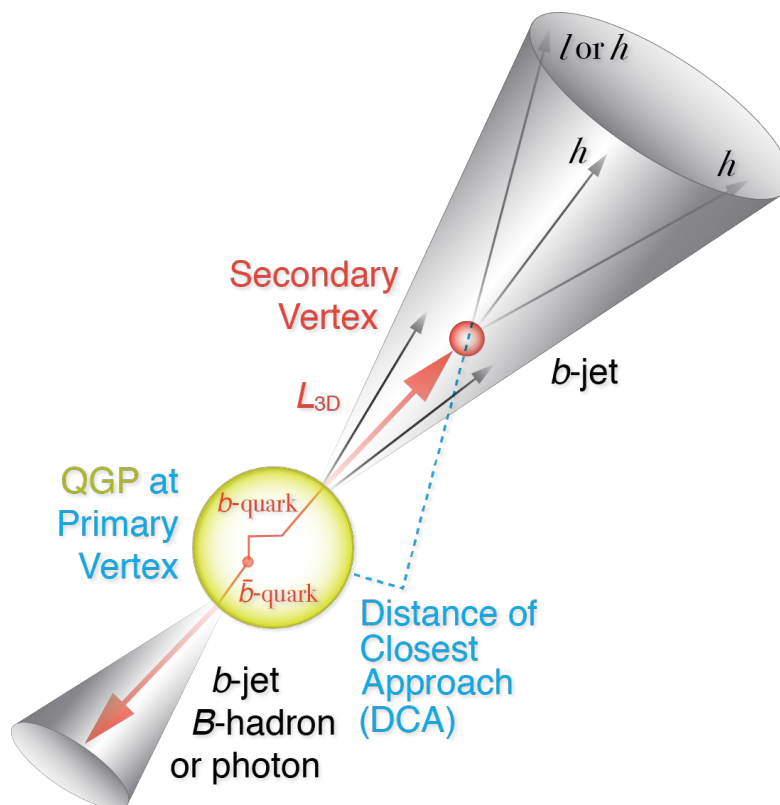


# 2 Heavy Flavor Jet Simulation 3 and Analysis

4 Anthony Frawley, Jin Huang, Xuan Li, Sanghoon Lim,  
5 Ming Liu, Mike McCumber, Darren McGlinchey,  
6 Gaku Mitsuka, Dennis Perepelitsa, Cesar da Silva,  
7 Haiwang Yu, (welcome your contribution too)

8 Version v1.0, June 30, 2017



9     **Notes to collaborators:**

- 10     • Your comments will be appreciated.
- 11     • Please include the version of the note (on cover page) and line number
- 12         in your comment. Separating comments by chapters would also help us
- 13         distribute it to primary chapter authors.
- 14     • Please send your comments to [sph-hf-2017-001-l@lists.bnl.gov](mailto:sph-hf-2017-001-l@lists.bnl.gov).

15     **Notes to authors:**

- 16     • Please use Luminosity assumption in Section [1.3](#).
- 17     • Please use sPHENIX style for your plots: [https://github.com/sPHENIX-Collaboration/](https://github.com/sPHENIX-Collaboration/macros/tree/master/macros/sPHENIXStyle)
- 18         [macros/tree/master/macros/sPHENIXStyle](https://github.com/sPHENIX-Collaboration/macros/tree/master/macros/sPHENIXStyle)

# Contents

20	<b>1 Introduction</b>	<b>1</b>
21	1.1 Physics Goals . . . . .	1
22	1.2 Detector Setup . . . . .	2
23	1.3 Luminosity and acceptance assumptions . . . . .	4
24	1.4 Overview for $b$ -jet studies at sPHENIX . . . . .	4
25	<b>2 Event generation and inclusive <math>b</math>-jet projection</b>	<b>8</b>
26	2.1 Simulation setup . . . . .	8
27	2.2 $b$ -jet cross section . . . . .	9
28	2.3 $b$ -jet nuclear modification . . . . .	10
29	<b>3 <math>b</math>-jet tagging: track-counting algorithm</b>	<b>12</b>
30	3.1 Introduction . . . . .	12
31	3.2 Simulation and Analysis Setup . . . . .	12
32	3.3 Results . . . . .	13
33	3.3.1 $b$ -jet tagging without MVTX . . . . .	13
34	3.3.2 $b$ -jet tagging for sPHENIX with MVTX upgrade . . . . .	14
35	<b>4 <math>b</math>-jet tagging: secondary vertex in jet</b>	<b>17</b>
36	4.1 Introduction . . . . .	17
37	4.2 Simulation and Analysis Setup . . . . .	17
38	4.3 Results . . . . .	19
39	<b>5 di-<math>b</math>-jet correlations</b>	<b>24</b>
40	5.1 Introduction . . . . .	24
41	5.2 Simulation and Analysis Setup . . . . .	24
42	5.3 Results . . . . .	26
43	<b>6 Exploring <math>b</math>-jet-<math>B</math>-meson correlations</b>	<b>28</b>
44	6.1 Introduction . . . . .	28
45	6.2 Simulation and Analysis Setup . . . . .	29
46	6.3 Results (Internal discussion use only) . . . . .	29
47	<b>7 Final words</b>	<b>32</b>

# Chapter 1

## Introduction

### 1.1 Physics Goals

Heavy flavor (HF) quarks ( $c$ ,  $b$ ) play a unique role for studying the QCD in vacuum as well as at finite temperature or density. Their masses are much larger than the QCD scale ( $\Lambda_{\text{QCD}}$ ), the additional QCD masses due to chiral symmetry breaking, as well as the typical medium temperature created at RHIC and LHC. Therefore they are created predominantly from initial hard scatterings and their production rates are calculable in perturbative QCD. They are thus calibrated probes that can be used to study the QGP in a controlled manner.

The planned sPHENIX baseline detectors with the proposed Monolithic Active Pixel Sensor Vertex Detector (MVTX) upgrade will enable a much desired heavy-flavor physics capability in QGP studies, extending present RHIC measurements to much broader transverse momentum range and providing access to critical but uncharted parameter space of QGP properties. In combination with the sPHENIX calorimetric jet reconstruction, the MVTX provides a particularly important new capability to sPHENIX baseline program - the identification of jets originating from heavy quarks from low to high  $p_T$ . In this note, we investigate the detection capability and physics reach of the  $b$ -jet program at sPHENIX via simulation and analysis. This particular measurement represents both a new opportunity at RHIC and an example of complementarity to the LHC: the projected sPHENIX measurement both extends the LHC measurement to lower transverse momenta and provides a kinematic overlap, where the same jets can be studied in the different QGP conditions at RHIC and LHC.

Compared to HF hadrons, measurements of jets provide more information on the initial parton kinematics and the nature of parton interactions with the QGP medium. The evolution of parton showers probes the coupling with the medium over a range of scales, providing sensitivity to its scale-dependent microscopic structure. Jets containing  $b$ -quarks are of particular interest, as Bottom quarks, which are  $\sim 1000$  times heavier than the light quarks, produce unique energy loss signatures due to their large mass ( $4.2 \text{ GeV}/c^2$ ). At momenta

comparable to this scale, bottom quarks will preferentially lose energy via collisions with the plasma quasi-particles and not via gluon radiation, which is predominant for light quarks. Jets containing  $b$ -quarks are also distinct from light-quark jets in their high multiplicity and hard fragmentation, where the leading particle typically carries 70-80% of the jet energy.

Measurements of  $b$ -jets in Pb+Pb collisions at LHC cover momenta larger than 80 GeV/ $c$  [6, 8]. Surprisingly, these measurements indicate a nuclear modification factor very similar to inclusive jets [6]. One of the explanations is that the mass of the  $b$ -quark is small when compared with the jet transverse momenta,  $p_T \geq 80$  GeV/ $c$ . The other hypothesis is that given that most of  $b$ -jets at LHC are from gluon splitting processes, the jet containing a  $b$ -quark still behaves as a massive color octet object when crossing the medium, resembling a massive gluon [9]. In comparison, RHIC measurements are complimentary, and has the following advantages:

- $b$ -jets can be measured with momentum as low as 15 GeV/ $c$ , where the quark mass is more important for the energy loss mechanisms.
- the main process producing  $b$ -jets at RHIC is the leading order gluon fusion ( $g + g \rightarrow b + \bar{b}$ ) and excitation of intrinsic  $b$ -quarks in the proton wave function ( $b + g \rightarrow b + g$ ). Therefore,  $b$ -jet at RHIC are less contaminated by the gluon splitting channel, which is estimated to be below 15% using a PYTHIA8 simulations [2].

## 1.2 Detector Setup

In this section, we discuss the relevant tracking detector performance of sPHENIX experiment, including MVTX (alternatively noted as MAPS), Intermediate tracker (INTT or IT), and Time projection chamber (TPC). In particular, the MVTX, as shown in Figure 1.1, is the key upgrade to sPHENIX in order to provide the precision measurement of the primary vertex as well as the displaced secondary tracks from heavy quark decays. A full detector GEANT4 display is also shown in Figure 1.2.

In this note, we used cylindrical shape to approximate the geometry the tracking detector in the GEANT4 detector model. Proper material and pixel size is assigned on each layer to reproduce the average multiple scattering and cluster position resolution at each tracking layer. A Hough-transform based pattern recognition and Kalman-filter based track fitting algorithms were employed for track finding and fitting, respectively.

Figure 1.3 shows the single track efficiency and the DCA pointing resolution in the bending plane as a function of  $p_T$  based on the full GEANT4 detector simulation plus the offline tracking software reconstruction. The efficiencies were evaluated using charged pion tracks embedded in central HIJING Au+Au events (i.e., highest multiplicity in sPHENIX). The single track efficiency is about 80% at 1 GeV/ $c$  and the DCA pointing resolution is about 40  $\mu\text{m}$  for 0.5–1 GeV/ $c$  tracks. These performance parameters meet detector requirements.

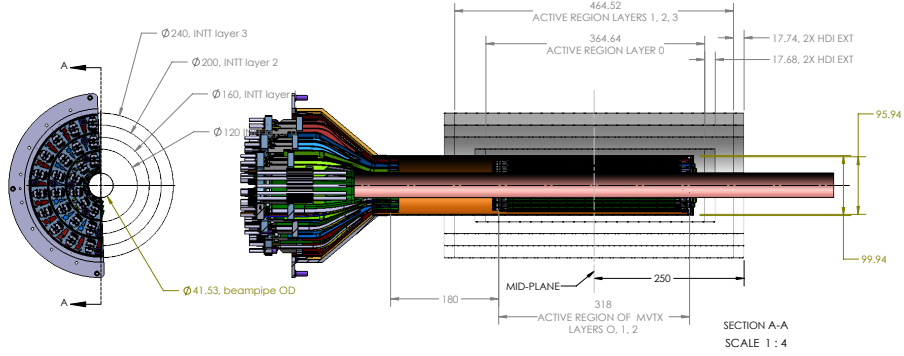


Figure 1.1: sPHENIX vertex detectors. Beam view of MVTX detector on the left, and side view of MVTX and INTT on the right.

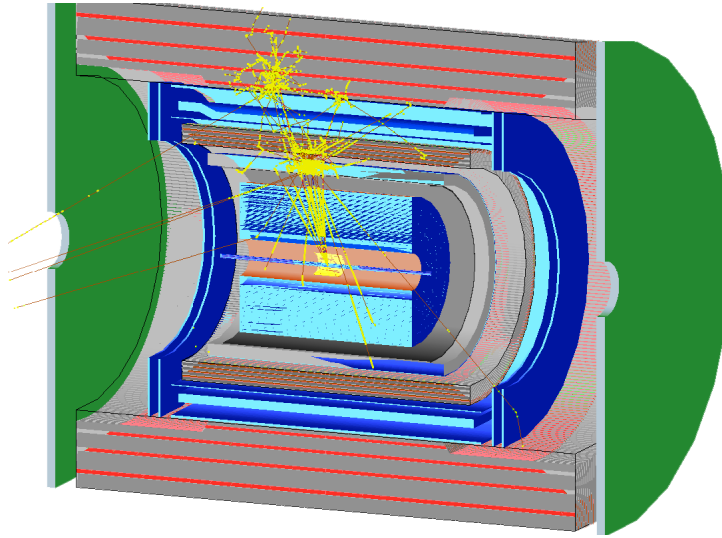


Figure 1.2: a  $p_T = 30 \text{ GeV}/c$   $B$ -meson showers in sPHENIX detector, as simulated in GEANT4.

121 The collaboration is finalizing on a new tracking simulation setup, which  
 122 employ realistic detector geometry models in GEANT4 and GENFIT2-based  
 123 pattern recognition and fitting modules. Although it is not yet used in  $b$ -jet  
 124 simulation study of this note, we expect this new simulation be employed for  
 125  $b$ -jet studies soon and provide improved simulation and performance.

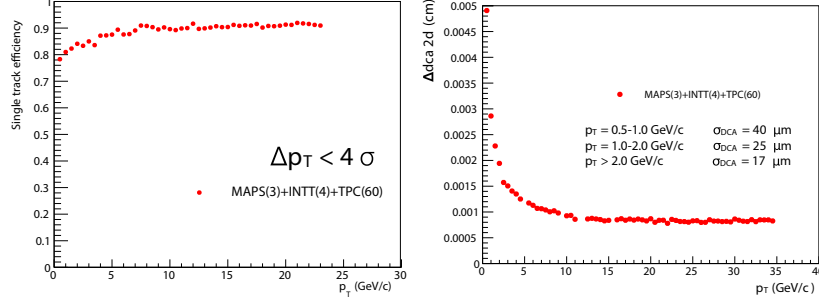


Figure 1.3: Single track reconstruction efficiency (left) and DCA pointing resolution in the bending plane (right) in central Au+Au collisions from full HIJING plus GEANT4 simulation.

### 1.3 Luminosity and acceptance assumptions

The five-year sPHENIX run plan as lined out in note sPH-TRG-000 [13] is used for projection in this note, which includes the following collision systems:

**$p+p, \sqrt{s} = 200$  GeV:** sampling  $200 \text{ pb}^{-1}$  with jet patch trigger, which is rounded up from  $197 \text{ pb}^{-1}$  as in sPH-TRG-000 [13].

**Au+Au,  $\sqrt{s} = 200$  GeV:** for  $b$ -jets with  $p_T < 30 \text{ GeV}/c$ , we assume 240 Billion MB Au+Au collision, which is rounded up from 239 Billion MB Au+Au collision as in sPH-TRG-000 [13]. For  $b$ -jets with  $p_T > 30 \text{ GeV}/c$ , we assume 550 Billion Au+Au collision sampled using a jet patch trigger of moderate rejections.

**$p+\text{Au}, \sqrt{s} = 200$  GeV:**  $0.33 \text{ pb}^{-1}$  with jet patch trigger or 0.6 trillion sampled collisions.

For all collision systems, we use full acceptance for  $R = 0.4$  jet in the sPHENIX calorimetry and tracking acceptance of  $|\eta_{\text{detector}}| < 1.1$ , i.e.

$$|\eta_{b\text{-jet}}| < 0.7$$

For vertex ranges, we assume usable  $|v_z| < 10 \text{ cm}$ . In this range, MVTX detector provides at least two hits in  $|\eta| < 1$  and therefore leads to a full coverage for DCA measurement in the full jet cone.

### 1.4 Overview for $b$ -jet studies at sPHENIX

Detection of  $b$ -jets with the sPHENIX detector is complicated by the comparative rarity of  $b$ -jets (Section 2.2), and also by the significant background of the underlying event in heavy ion collisions. Multiple exploratory methods have

been developed to demonstrate that the planned sPHENIX detector with the proposed MVTX upgrade allows  $b$ -jet tagging in sPHENIX and to enable cross checks of the expected systematic uncertainties. As shown in the right diagram of Figure 1.4, these methods are based on the unique features of  $B$ -hadron decays, including the finite decay length and leptonic decay products. These methods are:

- Identify  $b$ -jets by requiring multiple tracks within the jet cone that do not originate from the primary collision vertex. These are likely be the long-lived  $B$ -hadron decay products. As an initial study, we performed a full sPHENIX detector simulation to demonstrate such capability as discussed in Chapter 3. Despite the simplified algorithm used in this exploration, the  $b$ -tagging performance approaches that seen by CMS in their  $b$ -jet analysis at much higher energy [8, 6]. Additional techniques will be deployed in the final software package to further optimize performance, including likelihood analyses, 3-dimensional track displacement and machine learning techniques.
- Identify  $b$ -jets by requiring that multiple tracks within the jet cone come from the same displaced secondary vertex distinct from the primary vertex. This method is related to the previous one; however it also uses the knowledge that a  $B$ -hadron is likely to decay into multiple daughter particles. This provides additional power in selecting and cross checking  $b$ -jet candidates identified via the first method. We also demonstrated this method in full simulation as discussed in Chapter 4. This method also provide data driven quantification of  $b$ -jet purity via secondary vertex kinematics fitting.
- Identify  $b$ -jets by requiring that electron or positron tracks are detected within the originally identified jet cones. Utilizing the fact that  $B$ -hadrons have a significant chance ( 20%) to decay to a leptonic final state, this is a nearly orthogonal method that could provide an independent cross check of both methods above. Although not included in this note, We plan to explore its feasibility in the sPHENIX environment and performance projections for such cross checks.

After the initial identification of  $b$ -jet candidates, the purity of  $b$ -jets in the candidate sample will be quantified in a data-driven way using the invariant mass and transverse momentum of the secondary vertex, which has proven to be critically important in the LHC environment [8, 6]. The projected uncertainty of the nuclear modification of inclusive  $b$ -jet is shown in Figure 2.2 in Chapter 2, which places stringent tests on the models describing the coupling between heavy quarks and the QGP [9]. We are in close collaboration with theory groups to update the model predictions of inclusive  $b$ -jet nuclear modification at the RHIC energy in the sPHENIX kinematic region.

Beyond the inclusive  $b$ -jet nuclear modification measurement, additional techniques in jet substructure and correlation studies will be performed. Inclusive  $b$ -jets can originate from a high-energy  $b$ -quark (a true  $b$ -quark jet) or



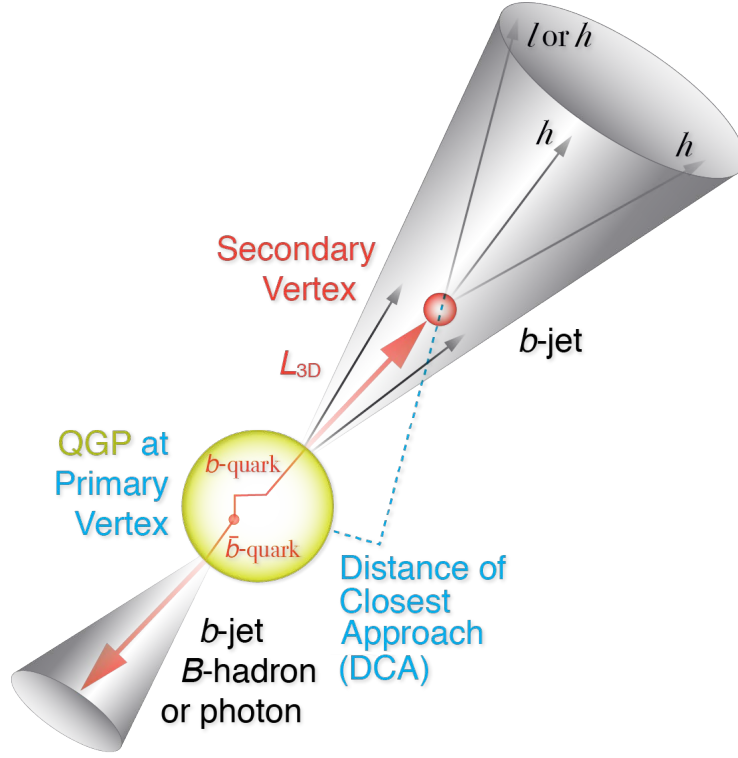


Figure 1.4: A  $b$ -quark traverses the QGP and fragments into a  $b$ -jet. The principles of tagging the rare  $b$ -jets are based on unique features of  $B$ -hadrons: long life time and finite decay length of  $B$ -hadron ( $L_{3D} \sim \text{few mm}$ ), decay tracks from secondary vertices and leptonic decay products.

from a gluon that splits into  $b$ -quark and  $b$ -antiquark ( $g \rightarrow b\bar{b}$ -jet). These two categories of  $b$ -jets could potentially have very different interactions with the QGP, because in the latter case the correlated  $b$ -quark and  $b$ -antiquark traverse coherently through the QGP in a color octet state with twice the  $b$ -quark mass [9]. Although inclusive  $b$ -jets at RHIC are expected to be dominated by the  $b$ -quark jets [14], the remaining  $g \rightarrow b\bar{b}$ -jet component could complicate the interpretation the inclusive  $b$ -jet results. sPHENIX will allow us to discriminate these two categories of  $b$ -jet productions and provide cleaner access to the dynamics of high energy  $b$ -quark interactions with the QGP:

- Correlation studies for  $b$ -jets: the fraction of true  $b$ -quark jets can also be enhanced by selecting  $b$ -quark partonic production channels. This is achieved by requiring the  $b$ -jet candidate to be correlated with another  $b$ -jet,  $B$ -hadron, or photon in the same event [10], as illustrated in Figure 1.4. In particular, correlations between two  $b$ -jets can be measured with high statistics using the MVTX and sPHENIX detectors, taking advantage of

their high rate capability and their large instrumented acceptance (covering nearly 80% of produced di-jets [2]). The projection for the transverse momentum balance of  $b$ -jet-pairs is discussed in Chapter 5. A preliminary study for  $b$ -jet- $B$ -meson correlations is discussed in Chapter 6.

- Jet substructures: in recent years, the field of high-energy physics has developed a set of techniques to inspect the substructure of jets, to tag boosted objects and to differentiate between gluon and quark jets. These techniques have recently been adopted to study the interplay between light-jet probes with the QGP medium at the LHC [7] and at RHIC [11]. These techniques can also be utilized in identifying true  $b$ -quark jets for sPHENIX. Specifically, so-called jet grooming algorithms will be used to remove soft radiation from the jet, and to identify two leading subjet structures that correspond to the earliest splitting of the initiating parton [12]. In the leading order picture, the transverse momentum of the two subjets is likely to be similar in a  $g \rightarrow b\bar{b}$ -jet, and in true  $b$ -quark jets, one subjet would likely dominate. Therefore, a measurement of transverse momentum ratio of the two subjets will be used to identify and quantify the purity of the true  $b$ -quark jets. A secondary vertex that is found by the MAPS detector that associates with the subjets can further confirm the  $b$ -quark origin of the subjets.

## Chapter 2

# Event generation and inclusive $b$ -jet projection

### 2.1 Simulation setup

A PYTHIA8 based simulation using Hard QCD mode,  $\hat{q}_T = 7$  GeV/c, and CTEQ6L PDF was used to simulate  $b$ -jet production rate in sPHENIX. The relevant part of PYTHIA8 configuration file is as following:

```
! phpythia8.cfg for b-jet simulation
! Beam settings
Beams:idA = 2212    ! first beam, p = 2212, pbar = -2212
Beams:idB = 2212    ! second beam, p = 2212, pbar = -2212
Beams:eCM = 200.    ! CM energy of collision
! PDF
PDF:pdfSet = 7 ! CTEQ6L, NLO alpha_s(MZ) = 0.1180.
! Process
HardQCD:all = on
! Cuts
PhaseSpace:pTHatMin = 7.0
```

[9] found PYTHIA8 + CTEQ6L reproduced the  $b$ -jet cross section in LHC data at  $\sqrt{s} = 7$  TeV. The  $b$ -jet and inclusive jet production rate at the RHIC energy is also checked in Section 2.2.

After the PYTHIA8 simulation, the produced particle goes through truth jet finding, which utilized the anti- $k_T$  algorithm in FASTJET package with a parameter of  $R = 0.4$ . Then, the jet partonic flavor is tagged, which mark the flavor of the jet as the flavor of heaviest quark inside the jet-cone. An alternative definition using heaviest-quark meson inside the jet cone is also available in the

255 tagger output, but NOT used in this analysis. The tagger setup is committed  
 256 to the analysis repository at [https://github.com/sPHENIX-Collaboration/](https://github.com/sPHENIX-Collaboration/analysis/tree/master/HF-Jet/TruthGeneration)  
 257 [analysis/tree/master/HF-Jet/TruthGeneration](https://github.com/sPHENIX-Collaboration/analysis/tree/master/HF-Jet/TruthGeneration).

258 A branch of macros repository that execute this setup can be found at [https://github.com/blackcathj/macros/tree/SinglePart\\_master\\_prod\\_pythia\\_](https://github.com/blackcathj/macros/tree/SinglePart_master_prod_pythia_truth_Bjet_MB/macros/g4simulations)  
 259 [truth\\_Bjet\\_MB/macros/g4simulations](https://github.com/blackcathj/macros/tree/SinglePart_master_prod_pythia_truth_Bjet_MB/macros/g4simulations).  
 260

261 This event procedure should be cross checked with other choices event  
 262 generators, e.g. MC@NLO, which is not yet performed in this note.

## 263 2.2 *b*-jet cross section

264 For this cross section estimation,  $53 \text{ pb}^{-1}$  of PYTHIA8 simulation was performed  
 265 with the above setup. As shown in Figure 2.1, the result inclusive jet and *b*-jet  
 266 cross section are compared with PHENIX data [3] and FONLL calculations [5, 4],  
 267 respectively. The *b*-jet purity before tagging is around 0.5% of the inclusive jets.

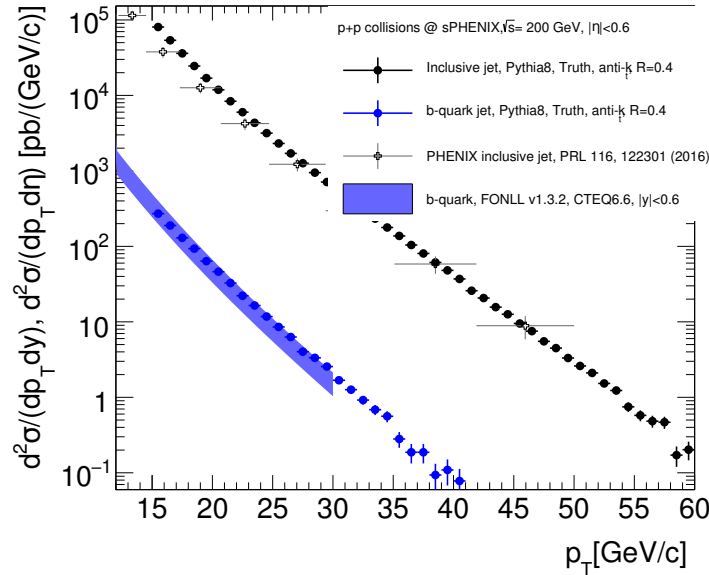


Figure 2.1: Comparison of the cross section for *b*-jets (blue) and all jets (black). They are consistent with the published inclusive jet cross section [3] and the *b*-bare-quark production cross section from a FONLL calculations [5, 4], respectively. *b*-jets are rare compared to the much more abundant light quark jets.

268 The source code generating this estimation is located at `DrawCrossSection()`  
 269 in `Draw_HFJetTruth.C` as linked here

## 2.3 $b$ -jet nuclear modification

The projected statistical uncertainty for nuclear modification factor in 0-10% Au+Au collisions are shown in Figure 2.2. The jet pseudorapidity is constrained within  $|\eta| < 0.7$ , which allows full  $R = 0.4$ -jet cone be contained within tracking and calorimetry coverage for all the vertex ranges. Based on the  $b$ -jet tagging performance studies in Chapter 3 and 4, an optimistic but plausible purity and efficiency for  $p+p$  and central Au+Au purity and efficiency are assumed for this estimation, i.e. 40% purity at 60% efficiency in  $p+p$  collisions and 40% purity at 40% efficiency in central Au+Au collisions.

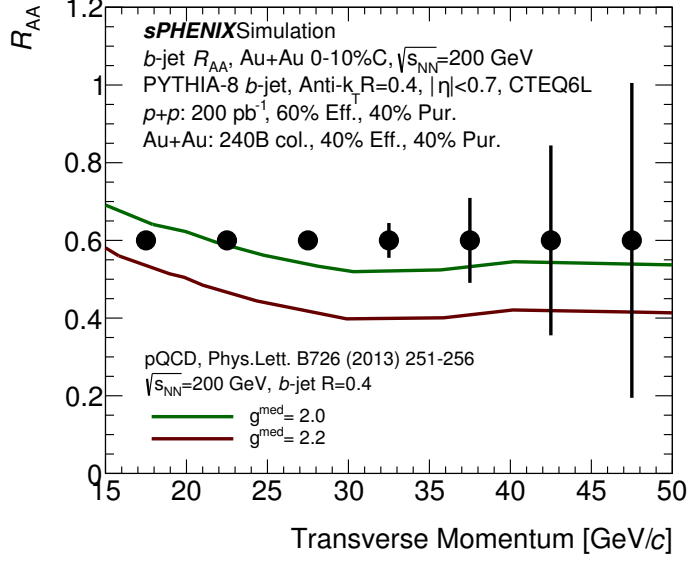
Two trigger scenarios are considered:

- Figure 2.2a is assuming untriggered recorded sample of 240 B MB Au+Au collisions.
- Since the uncertainty is only visible for  $b$ -jets with  $p_T > 30$  GeV/ $c$ , a moderate jet trigger is further assumed to allow sampling the full 550 Au+Au collisions in the MVTX vertex range of  $|z| < 10$  cm (more in Section 1.3), which leads to Figure 2.2b.

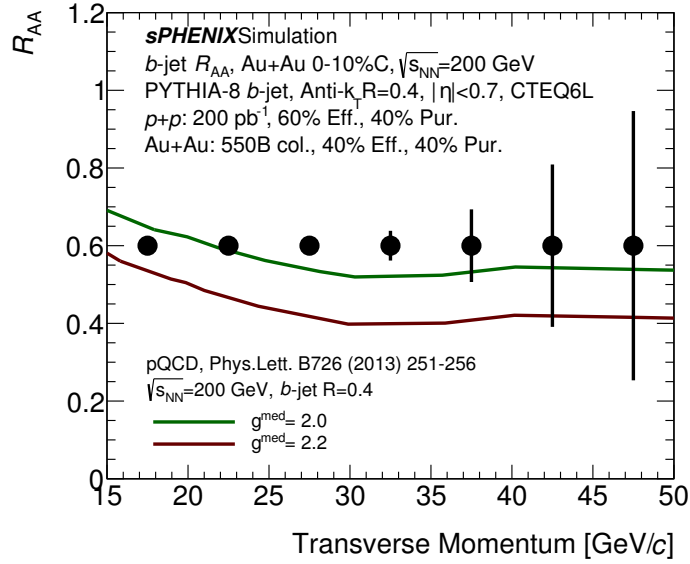
The difference in uncertainty projection between these two scenarios are minor since the uncertainty of  $R_{AA}$  for inclusive  $b$ -jets are dominated by the  $p+p$  statistics. Meanwhile, high Au+Au statistics are highly demanded for the jet correlation measurements in Chapter 5 and 6.

The result show good statistical precision covering  $b$ -jet in kinematics range of  $15 < p_T < 40$  GeV/ $c$ . This data will provide precision constraint on the  $b$ -quark counting constant to QGP as valuated in a heavy quark transport model [9], which is now reevaluated at RHIC energy under the support of LANL MVTX LDRD program.

The source code generating this estimation is located at `CrossSection2RAA()` in `Draw_HFJetTruth.C` as linked here



(a)



(b)

Figure 2.2: Statistical projection of sPHENIX inclusive  $b$ -jet data in terms of the nuclear suppression factor (black circles), which is compared with QGP transport models for  $b$ -quark jets evaluated at the RHIC energy with two possible coupling strength (curves) [9]. (a) is assuming untriggered recorded sample of 240 B MB AuAu collisions, and (b) assumes sampled 550 B Au+Au collisions using a moderate jet trigger.

## Chapter 3

# *b*-jet tagging: track-counting algorithm

### 3.1 Introduction

For the track counting method, we identify *b*-jets by requiring multiple tracks within the jet cone that do not originate from the primary collision vertex. These are likely be the long-lived *B*-hadron decay products when compared with light-quark jets and *c*-jets. In this first implementation, we required one, two or three tracks satisfies the significance cut. This algorithm is first developed in the proposal stage of sPHENIX [2], which is now implemented in full GEANT4 tracking simulations. The future version of this algorithm will employ a likelihood method to utilize full information content of tracks.

### 3.2 Simulation and Analysis Setup

As an initial study, we performed a full sPHENIX detector simulation to demonstrate such *b*-jet tagging capability using the track counting algorithm. The simulation set up includes following components:

- Using generator setup in Section 2.1
- Jet reconstruction: FASTJET on the generated particles (`TruthJetInput (Jet::PARTICLE)`);  $R = 0.4$
- Flavor tagging: Using the Jet flavor tagger: `HFJetTruthTrigger` as discussed in Section 2.1
- Tracking. Using cylindrical MVTX(3) + INTT (4) + TPC(60), where numbers in the bracket denote number of layers in each tracking detector. To demonstrate the importance of MVTX upgrade, this study was also performed without MVTX for comparison. Using `PHG4HoughTransformTPC`

as the pattern recognition module; using PHG4TrackKalmanFitter as the fitting module. For *DCA* calculations, we used RAVE package [1] to reconstruct the primary vertex. The method `avf-smoothing:1` was used in this study.

- The **BJetModule** was used to extract useful information in the DST Node-Trees and create a compact TTree with truth, jet, track information. The plotting macro in the `macros` folder in this package was used to summarize and do the plotting.
- tracks inside each jet are sorted according to the highest  $DCA/\sigma(DCA)$  above 0. A jets is tagged as a *b*-jet candidate if the one, two or three tracks are above a minimal cut on track's  $DCA/\sigma(DCA)$ , which leads to the performance curve as discussed in the next section.

### 3.3 Results

This section summarize performance results for *b*-tagging using the track counting algorithm. Two setups are considered, sPHENIX baseline without MVTX in Section 3.3.1, and sPHENIX with the MVTX upgrade in Section 3.3.2.

#### 3.3.1 *b*-jet tagging without MVTX

First, we performed *b*-jet tagging with INTT + TPC only, the results are shown in Figure 3.1 and Figure 3.2.

We could see from Figure 3.2, in this setup, even in the relative low occupancy *p*+*p* case, the INTT + TPC configuration is far below the targeted *p*+*p* working point of 60% efficiency 40% purity. Therefore, we do not feel the need to continue this reduced configuration into Au+Au studies, which involves with much higher multiplicity and background.

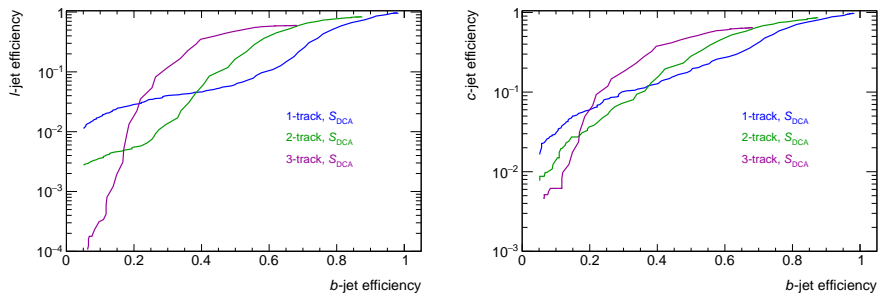


Figure 3.1: For the tracking configuration without the MVTX detector, the *l*(left)/*c*(right)-jet efficiency as a function of *b*-jet tagging efficiency in *p*+*p* collisions using the one-, two- and three-large DCA track methods.



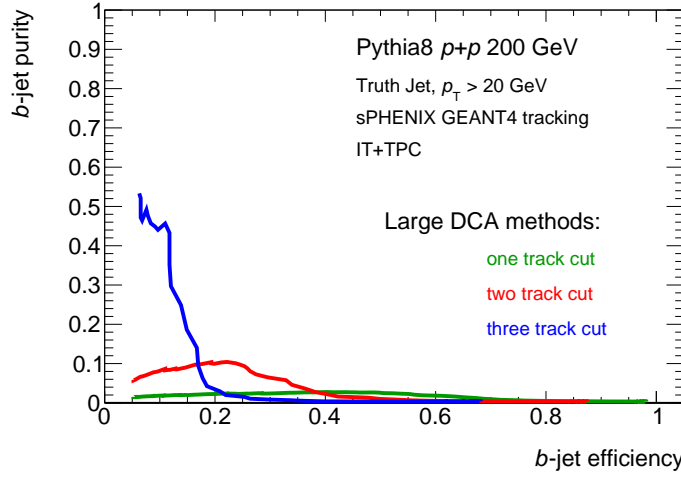


Figure 3.2: For the tracking configuration without the MVTX detector, the  $b$ -jet tagging performances in  $p+p$  collisions using the one-, two- and three-large DCA track methods. It is far below the targeted  $p+p$  working point of 60% efficiency 40% purity.

### 3.3.2 $b$ -jet tagging for sPHENIX with MVTX upgrade

Then we performed the  $b$ -jet tagging with the proposed tracking configuration of MVTX+INTT+TPC.

- The tagging performance results in  $p+p$  collisions as shown in Figure 3.3 and 3.4.
- PYTHIA8 jet events were also embedded into 0-10% central HIJING Au+Au collisions, which results in the tagging performance curve in the central Au+Au collisions as shown in 3.5 and 3.6.

Despite the simplified algorithm used in this exploration, the  $b$ -tagging performance approaches that seen by CMS in their  $b$ -jet analysis at much higher energy [8, 6]. Additional techniques will be deployed in the final software package to further optimize performance, including likelihood analyses, 3-dimensional track displacement and machine learning techniques.

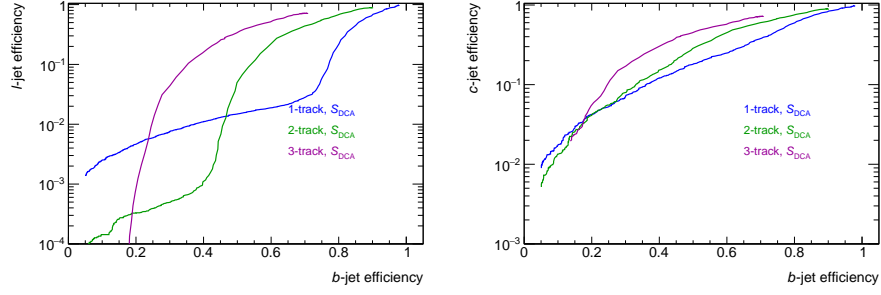


Figure 3.3:  $l$ (left)/ $c$ (right)-jet efficiency as a function of  $b$ -jet tagging efficiency in Au+Au collisions using the one-, two- and three-large DCA track methods with the MVTX detector.

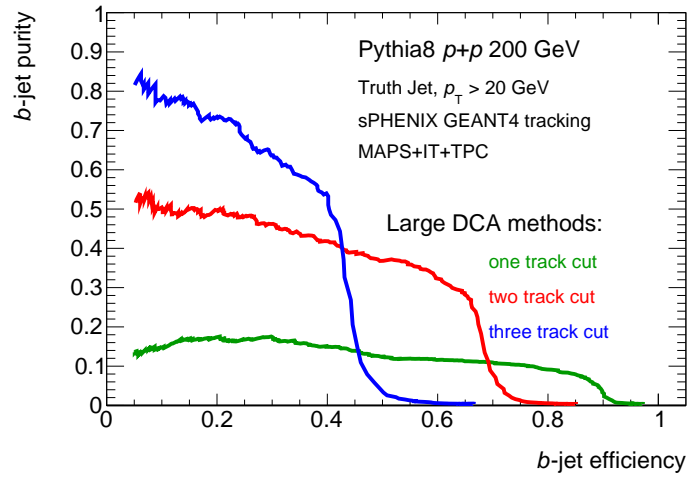


Figure 3.4: Projected  $b$ -jet tagging performances in  $p+p$  collisions using the multiple large DCA track method.

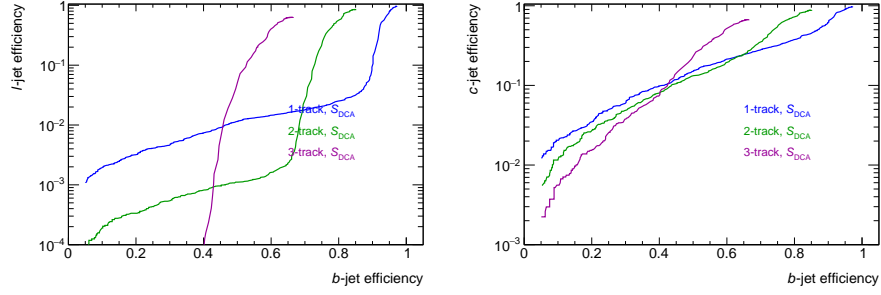


Figure 3.5: Projected  $l$ (left)/ $c$ (right)-jet efficiency as a function of  $b$ -jet tagging efficiency in  $p+p$  collisions using the one-, two- and three-large DCA track method with the MVTX detector.

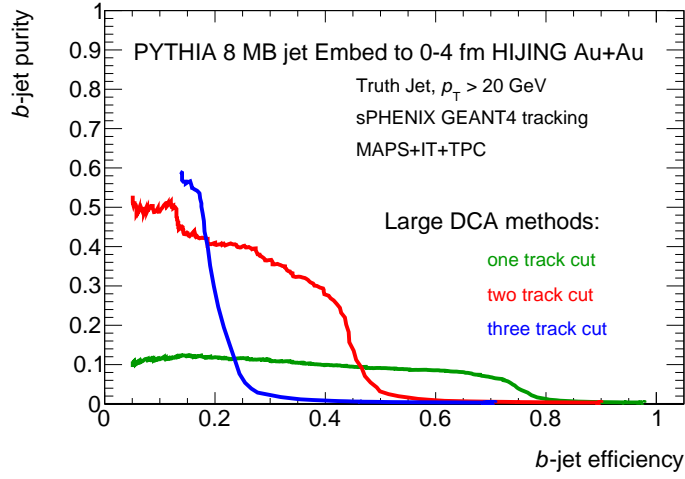


Figure 3.6:  $b$ -jet tagging performances in 0-10% central Au+Au collisions using the one-, two- and three-large DCA track methods. The tracking and tagging software is not yet fully optimized. Nevertheless, the performance curves allow an analysis working point of 30-40% purity at 30-40%  $b$ -jet efficiency as used in the existing analysis performed at LHC energy [6].

## Chapter 4

# *b*-jet tagging: secondary vertex in jet

### 4.1 Introduction

In this chapter, we identify *b*-jets by requiring that multiple tracks within the jet cone come from the same displaced secondary vertex distinct from the primary vertex. This method is related to the previous one; however it also uses the knowledge that a *B*-hadron is likely to decay into multiple daughter particles from a displaced common vertex. This provides additional power in selecting and cross checking *b*-jet candidates identified via the first method. This method is demonstrated in full simulation as discussed in this Chapter. This method also provides data driven quantification of *b*-jet purity via secondary vertex kinematics fitting.

### 4.2 Simulation and Analysis Setup

As an initial study for sPHENIX, we performed a full sPHENIX detector simulation to demonstrate such capability. The simulation set up includes following components:

- PYTHIA8 event generation with the configuration in Section 2.1, and all events are generated at  $(x,y,z)=(0,0,0)$ .
- Full GEANT4 detector response with all the tracking detectors (MVTX+INTT+TPC), which is represented in cylindrical geometry approximations.
- For performance evaluation in Au+Au collisions, hits of PYTHIA8 events are embedded into hits of central Au+Au collisions from HIJING and then input to GEANT4 simulation.
- Track reconstruction with the GENFIT2 package.

From the chain of PYTHIA8 + GEANT4 simulation and track reconstruction, DST files containing all reconstructed tracks are produced. A next analysis step to find secondary vertex is done with these DST files. The RAVE package developed by the CMS collaboration has been adopted in the sPHENIX software, and the GENFIT2 package for generalized Kalman Filter tracking provides interfaces to the RAVE. Therefore, reconstructed tracks with the GENFIT2 can be easily used for vertexing with the RAVE. The analysis step to reconstruct secondary vertex is following:

- Events containing at least one truth jet of  $p_T > 20 \text{ GeV}/c$  in  $|\eta| < 0.6$  are used in the secondary vertex finding, and flavor tagging of jets is done with the tagger introduced in Section 2.1.
- All reconstructed tracks of  $\chi^2/ndf < 5$  in a certain event are used for primary vertex finding, and the adaptive method for single vertex (avf-smoothing:1) is used.
- For each jet of  $p_T > 20 \text{ GeV}/c$  in  $|\eta| < 0.6$ , reconstructed tracks of  $\chi^2/ndf < 5$  within a jet cone ( $\Delta R < 0.4$ ) are used for secondary vertex finding. The adaptive method for multiple vertices (avr-smoothing:1) is used.
- Various  $p_T$  cuts are used to compare  $b$ -jet tagging performance among different contamination of soft particles.

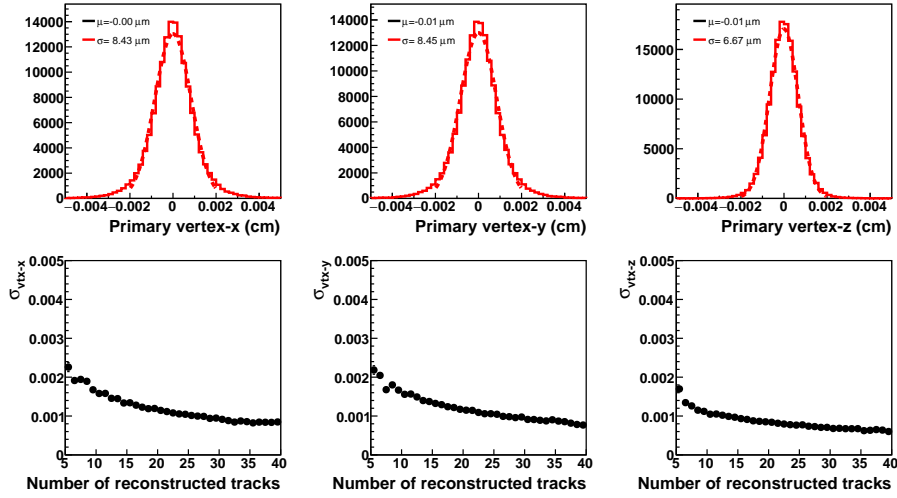


Figure 4.1: Primary vertex resolution of  $p+p$  events containing at least one jets of  $p_T > 20 \text{ GeV}/c$  in  $|\eta| < 0.6$  (top) and the resolution as a function of the number of reconstructed tracks (bottom).

From these procedure, primary and secondary vertices for each event are obtained. The primary vertex resolution of  $p+p$  events containing at least one

truth jet of  $p_T > 20 \text{ GeV}/c$  in  $|\eta| < 0.6$  is better than  $10 \mu\text{m}$  in all  $x$ ,  $y$ , and  $z$  directions as shown in Figure 4.1. The left panel of Figure 4.2 shows the number of secondary vertices per jet, and tracks inside a jet cone are used for finding secondary vertices. In case of light jet (black), most of jets have only one secondary vertex, but the chance of having more than one secondary vertex increases in charm and bottom jets which indicating decay vertex of charm and bottom hadrons. Even in light jets, multiple secondary vertex can be found due to decay of light mesons such as  $K^0$ . The right panel of Figure 4.2 shows secondary vertex mass of light jets in low mass region with an assumption of tracks are pions, and a clear peak of  $K^0$  is seen. The secondary vertex from  $K^0$  decay can be removed by applying mass cut ( $0.47 < M < 0.53 \text{ GeV}/c^2$ ) to increase purity of  $b$ -jets.

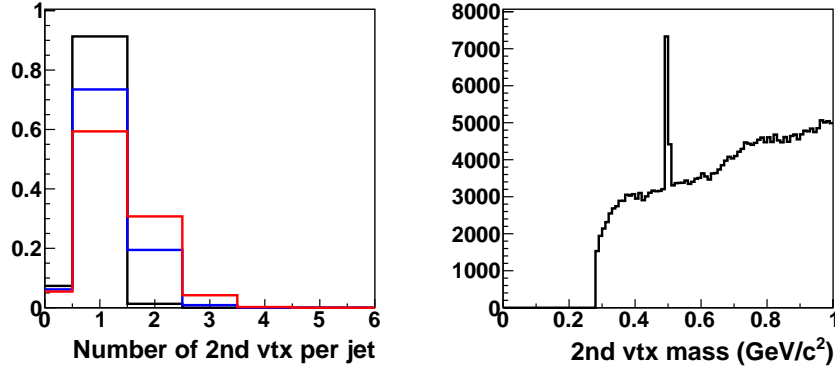


Figure 4.2: The number of secondary vertices per jet (left) and secondary vertex mass distribution from light jet in low mass region (right).

For each secondary vertex in a certain jet, the 3D flight distance from the primary vertex and its significance (distance divided by vertex error) is calculated, and the secondary vertex of most significant deviation is selected. Figure 4.3 shows the 3D flight distance of the secondary vertex of most significant deviation (left) and its significance (right). Each distribution is normalized to unity. The distributions from  $b$ -jets are much broader than the distribution from light jets which is basically due to decay vertex of long-lived  $b$ -hadrons. Based on these plot, the purity and efficiency of  $b$ -jet tagging can be evaluated.

### 4.3 Results

Based on the 3D flight distance significance shown in Figure 4.3,  $b$ -jets can be enriched by applying a large value of significance cut, but the efficiency will be decreased. The significance cut can be optimized based on the  $b$ -jet purity and efficiency. Figure 4.4 and 4.5 show light jet and  $c$ -jet efficiency as a function of  $b$ -jet tagging efficiency and rejection of different flavor jets as a function of

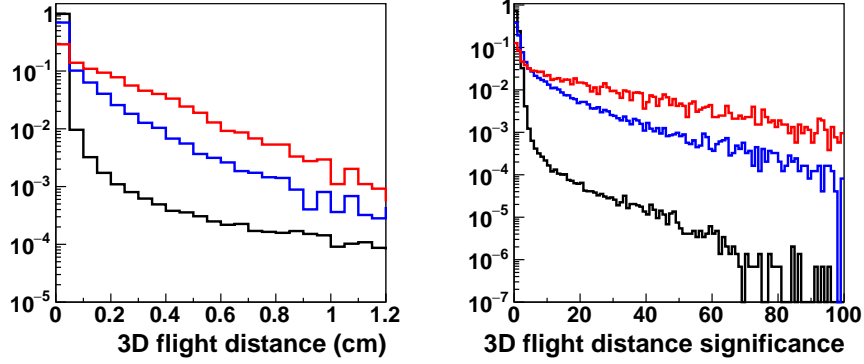


Figure 4.3: The 3D flight distance of the secondary vertex of most significant deviation (left) and its significance (right) for  $b$ -jets (red),  $c$ -jets (blue) and light jets (black).

the significance cut of 3D flight distance. Each secondary vertex should contain at least two good associated track, and a good associated track is defined as a track of weight in vertex determination is larger than 0.6. With this requirement, secondary vertices from uncorrelated tracks can be reduced. Figure 4.5 show the same set of plots in Figure 4.4, but the requirement of minimum number of associated tracks to a secondary vertex is three. When comparing the rejection plots (right) between Figure 4.4 and 4.5, initial rejection of light jets is much larger with the requirement of three minimum associated tracks.

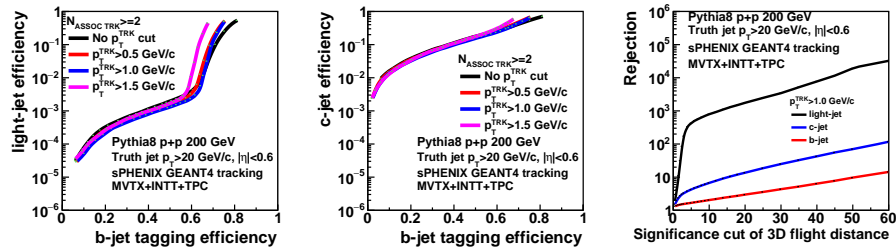


Figure 4.4: The efficiency of light jet (left) and  $c$ -jet as a function of  $b$ -jet tagging efficiency using secondary vertex method and rejection factors of different flavor jets as a function of significance cut of 3D flight distance of secondary vertex in  $p+p$  collisions. It is required to have at least two good associated tracks to each secondary vertex.

Figure 4.6 show  $b$ -jet purity versus efficiency with a requirement of minimum number of good associated tracks is two (left) or three (right). The  $b$ -jet purity is defined as a fraction of  $b$ -jet to all jets. Similarly with the results from the track counting method shown in Figure 3.4, a higher  $b$ -jet purity can be achieved

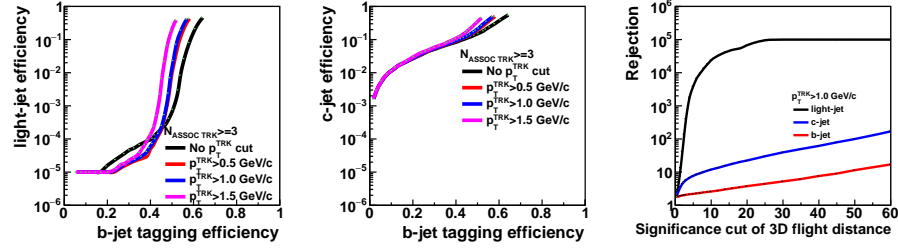


Figure 4.5: The efficiency of light jet (left) and c-jet as a function of  $b$ -jet tagging efficiency using secondary vertex method and rejection factors of different flavor jets as a function of significance cut of 3D flight distance of secondary vertex in  $p+p$  collisions. It is required to have at least three good associated tracks to each secondary vertex.

444 with a more strict cut, but the efficiency in low  $b$ -jet purity becomes lower.  
 445 Each plot include four distributions of various  $p_T$  cut for tracks. In case of the  
 446 minimum two associated tracks for a secondary vertex, the distribution of a  
 447 moderate  $p_T$  cut (blue,  $p_T > 1$  GeV/ $c$ ) shows a slightly better performance  
 448 than the distribution without any  $p_T$  cut (black). However, the  $b$ -jet efficiency  
 449 looks better without  $p_T$  cut in case of the minimum three associated tracks for a  
 450 secondary vertex.

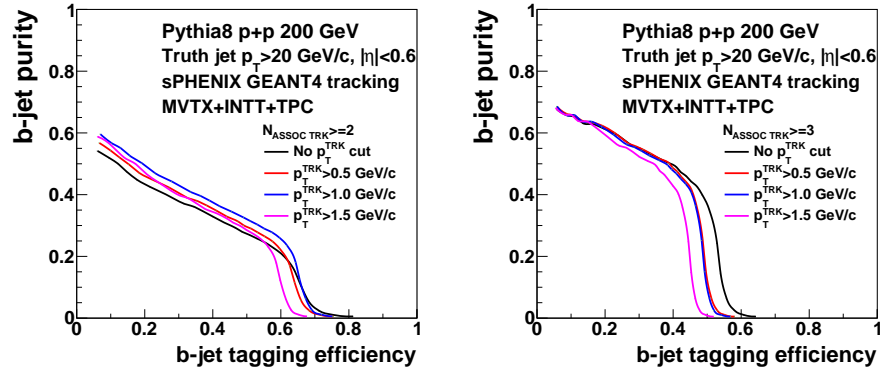


Figure 4.6:  $b$ -jet tagging performances in  $p+p$  collisions using secondary vertex method.

451 In order to evaluate  $b$ -jet tagging performance in central Au+Au colli-  
 452 sions, PYTHIA8 events are embedded into central Au+Au collision events from  
 453 HIJING as described in Section 4.2. Truth jet finding and flavor tagging are done  
 454 only with PYTHIA8 events. When finding secondary vertices, background parti-  
 455 cles from HIJING events around jets from PYTHIA8 events are included. In order  
 456 to remove background tracks which contribution is much larger than those in



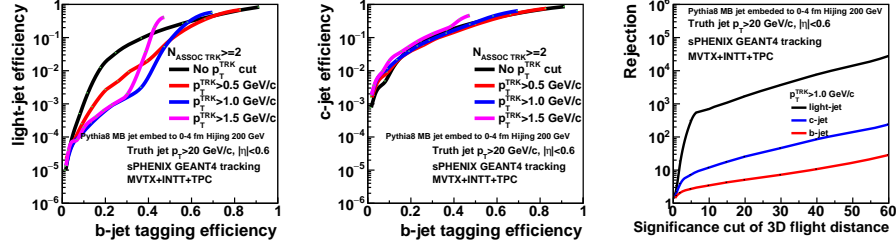


Figure 4.7: The efficiency of light jet (left) and  $c$ -jet as a function of  $b$ -jet tagging efficiency using secondary vertex method and rejection factors of different flavor jets as a function of significance cut of 3D flight distance of secondary vertex in central Au+Au collisions. It is required to have at least two good associated tracks to each secondary vertex.

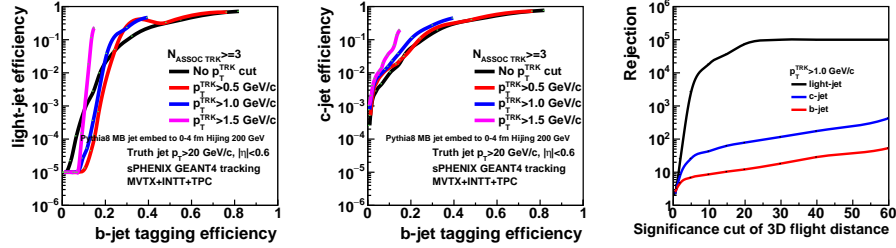


Figure 4.8: The efficiency of light jet (left) and  $c$ -jet as a function of  $b$ -jet tagging efficiency using secondary vertex method and rejection factors of different flavor jets as a function of significance cut of 3D flight distance of secondary vertex in central Au+Au collisions. It is required to have at least three good associated tracks to each secondary vertex.

457  $p+p$  collisions, a tighter track quality cut ( $\chi^2/ndf < 2$ ) is used. In addition,  
 458 tracks without MVTX hit are rejected which have a high chance of being fake  
 459 tracks in high multiplicity circumstance. Figure 4.4 shows the efficiency of light  
 460 jet and  $c$ -jet efficiency as a function of  $b$ -jet efficiency and rejection of different  
 461 flavor jets as a function of significance cut of secondary vertex 3D flight distance  
 462 with a minimum two associated tracks for each secondary vertex, and Fig. 4.5  
 463 show the same set of plots with a minimum three associated tracks for each  
 464 secondary vertex. Compared to the same plots in  $p+p$  collision shown in Fig. 4.4  
 465 and 4.5, a tighter significance cut is needed to achieve a similar light jet rejection  
 466 which results in a worse  $b$ -jet efficiency. Figure 4.9 shows the performance of  
 467  $b$ -jet tagging in central Au+Au collisions using secondary vertex method with  
 468 minimum two (left) or three (right) associated tracks per secondary vertex. At  
 469 this moment,  $b$ -jet efficiency around 40%  $b$ -jet purity is quite low, and we expect  
 470 to improve the  $b$ -jet tagging performance with updated tracking software in  
 471 near future.

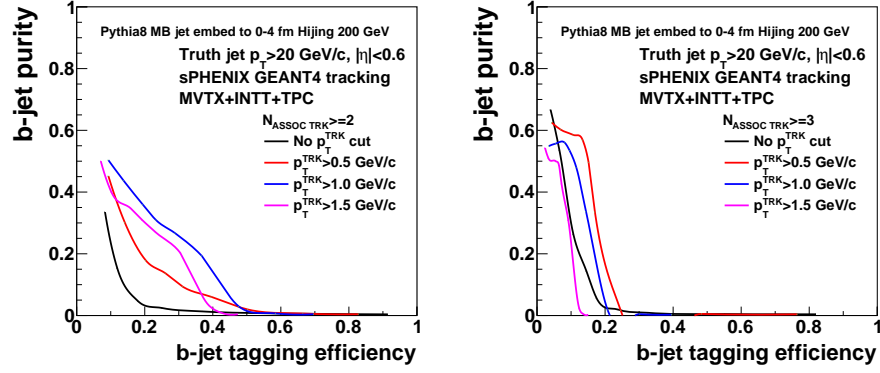


Figure 4.9:  $b$ -jet tagging performances in Au+Au collisions using secondary vertex method. The upper limit of all curves from both panels represents the best performance curve using various tunes of the secondary vertex method. We expect improved performance with as the tracking software being improved too.

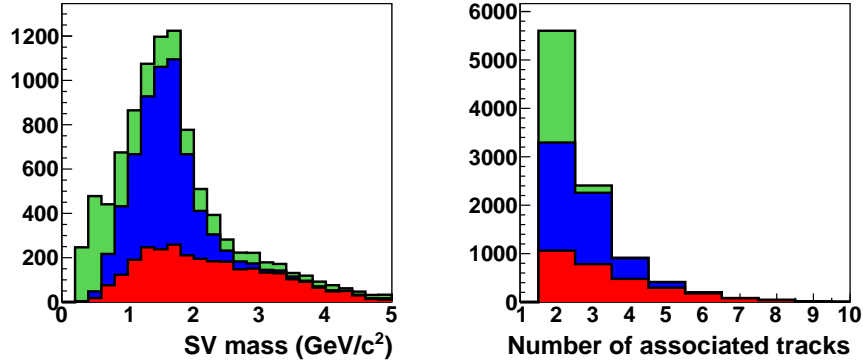


Figure 4.10: Secondary mass (left) and the number of associated tracks (right) distributions of light,  $c$ , and  $b$ -jets in  $p+p$  collisions.

472 After the initial identification of  $b$ -jet candidates, the purity of  $b$ -jets in the  
 473 candidate sample will be quantified in a data-driven way using the invariant  
 474 mass and transverse momentum of the secondary vertex, which has proven to  
 475 be critically important in the LHC environment [8, 6]. As shown in Figure 4.10,  
 476 secondary vertex of  $b$ -jet is likely have higher mass and higher number of  
 477 associated tracks. These distributions can be used for template fit on the  $b$ -jet  
 478 candidate sample to quantify its purity.

## Chapter 5

# di- $b$ -jet correlations

### 5.1 Introduction

Inclusive  $b$ -jets can originate from a high-energy  $b$ -quark (a true  $b$ -quark jet) or from a gluon that splits into a  $b$ -quark and  $b$ -antiquark ( $g \rightarrow b\bar{b}$ -jet). These two categories of  $b$ -jets could potentially have very different interactions with the QGP, because in the latter case the correlated  $b$ -quark and  $b$ -antiquark traverse coherently through the QGP in a color octet state with twice the  $b$ -quark mass [9]. Although inclusive  $b$ -jets at RHIC are expected to be dominated by the  $b$ -quark jets [14], the remaining  $g \rightarrow b\bar{b}$ -jet component could complicate the interpretation the inclusive  $b$ -jet results.

The fraction of true  $b$ -quark jets can also be enhanced by selecting  $b$ -quark partonic production channels. sPHENIX will allow us to do so by requiring the  $b$ -jet candidate to be correlated with another  $b$ -jet, as illustrated in Figure 1.4. In particular, correlations between two  $b$ -jets can be measured with high statistics using the MVTX and sPHENIX detectors, taking advantage of their high rate capability and their large instrumented acceptance (covering nearly 80% of produced di-jets [2]).

### 5.2 Simulation and Analysis Setup

The simulations for the di- $b$ -jet studies use the same PYTHIA8 configuration file detailed in Section 2.1 with the following exception:

```
PhaseSpace:pTHatMin = 10.0
```

As a first look, the analysis uses truth jet information only, where the truth jets are constructed using the FASTJET anti- $k_T$  algorithm with  $R = 0.4$ . PYTHIA8 events were first triggered on a  $b$ -jet with  $p_T > 10$  GeV/ $c$  and  $|\eta| < 2$  to be used for further analysis and cuts. Approximately 231 pb $^{-1}$  of effective  $p+p$  collisions were generated for use in this study. The basic cuts and assumptions used in the analysis are given in Table. 5.1.

Table 5.1: Analysis cut information for di- $b$ -jet study.

	$p+p$	Au+Au
cuts	$ \eta_{1,2}  < 0.7$	
	$p_{T,1} > 20 \text{ GeV}/c$	
	$p_{T,2} > 10 \text{ GeV}/c$	
	$ \Delta\phi_{12}  > 2\pi/3$	
	$ z  < 10 \text{ cm}$	
$b$ -jet Eff	60%	40%
$b$ -jet Purity	40%	40%
$b$ -jet $R_{AA}$		0.6

The  $b$ -jet efficiency, given in Table 5.1, is applied statistically to each  $b$ -jet in the event. It is likely that the tagging efficiency for the 2nd  $b$ -jet in the di- $b$ -jet event is significantly higher. However, since we don't have simulation studies of di- $b$ -jet efficiency (or purity), we choose to take the conservative approach. We apply an  $R_{AA} = 0.6$  factor only to the leading jet in the di- $b$ -jet, under the argument that, in the simplest approximation, if both jets loss same fraction of energy in the Au+Au collisions, the number of pair is reduced by  $R_{AA}$ . Since this is a pure truth simulation, the effects of the  $b$ -jet purity for the pair are non-trivial to properly estimate. For a conservative projection estimates, we assume that the purity increases the statistical errors by  $1/\sqrt{P}$  for each jet, where  $P$  is the purity. This effect occurs on both  $b$ -jets, and therefore is squared on the di- $b$ -jet measurements. The purity is not applied statistically on a jet-by-jet basis, but rather implemented as a scaling of the statistical uncertainties on the  $x_j$  distribution. The work on quantifying the di- $b$ -jet pair purity and efficiency in full GEANT4 simulation is still on-going and the result are expected for next revision of this study.

After applying the statistical efficiency effects and, in the case of the Au+Au, the  $R_{AA}$ , we find the following number of di- $b$ -jet:

- $p+p$  ( $200 \text{ pb}^{-1}$ ): 2868
- Au+Au ( $236 \text{ pb}^{-1}$ ): 897

In both cases, the distribution of  $x_j = p_{T,2}/p_{T,1}$  for  $b$ -jet pairs is calculated. The statistical errors on each point are then scaled by  $1/P$  to take the effect of the purity into account. In the case of the Au+Au, the statistical errors are additionally scaled by the ratio of the simulated nucleon-nucleon luminosity ( $236 \text{ pb}^{-1}$ ) to the desired nucleon-nucleon luminosity for the given centrality bin, given by Table 5.2. The  $\langle x_j \rangle$  is then calculated for  $p+p$ , and each centrality bin in Au+Au. The resulting uncertainties are shown in Table 5.2.

Table 5.2: The di- $b$ -jet  $\langle x_j \rangle$  for  $p+p$  and Au+Au collisions at  $\sqrt{s_{NN}} = 200$  GeV.

	$N_{evt}$	$N_{coll}$	$\int \mathcal{L}_{nn} dt [pb^{-1}]$	$\langle x_j \rangle$
$p+p$	–	–	200	$0.724 \pm 0.008$
Au+Au 0-10%	24.0B	962	549	$0.723 \pm 0.009$
Au+Au 10-20%	24.0B	603	344	$0.723 \pm 0.011$
Au+Au 20-40%	48.0B	296	338	$0.723 \pm 0.011$
Au+Au 40-60%	48.0B	94	107	$0.723 \pm 0.021$
Au+Au 60-92%	76.8B	15	27	$0.723 \pm 0.042$

### 5.3 Results

A preliminary projection of the transverse momentum balance,  $x_j$ , of  $b$ -jet pairs is shown in Figure. 5.1 for  $p+p$  and 0-10% central Au+Au collisions at  $\sqrt{s_{NN}} = 200$  GeV. These results are comparable in precision with recent results from Pb+Pb collision at  $\sqrt{s_{NN}} = 5.02$  TeV measured by the CMS collaboration [8]. Further, the projected uncertainties on the mean asymmetry,  $\langle x_j \rangle$ , as a function of  $N_{coll}$  is shown in Figure 5.2.

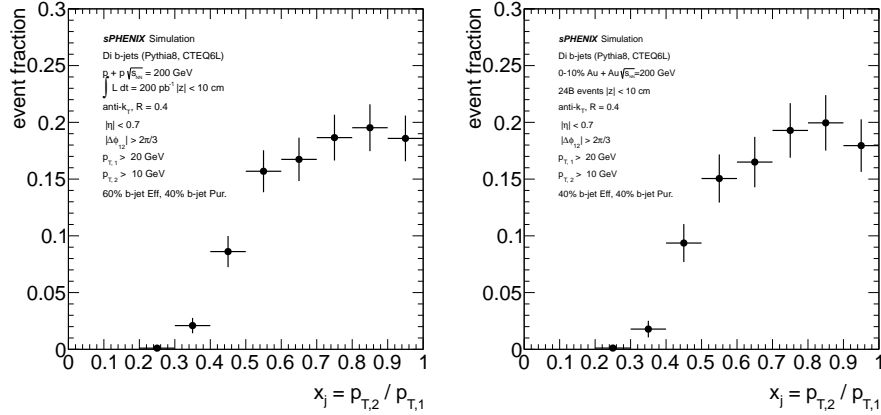


Figure 5.1: Preliminary projection of transverse momentum balance of  $b$ -jet pairs as enabled by sPHENIX and the MVTX upgrade, for  $p+p$  (left) and for 0-10% central Au+Au collisions at  $\sqrt{s_{NN}} = 200$  GeV (right).

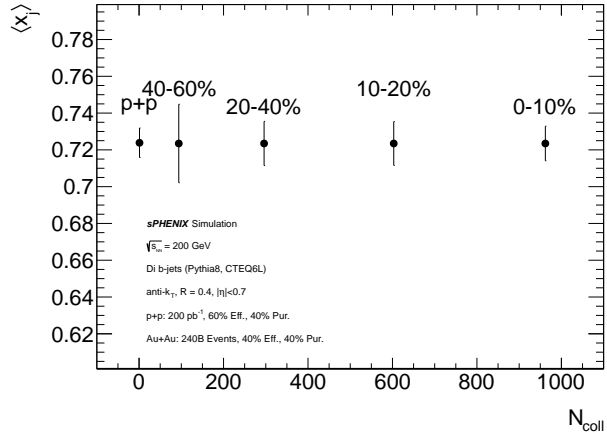


Figure 5.2: The mean di- $b$ -jet asymmetry,  $\langle x_j \rangle$  as a function of  $N_{\text{coll}}$  in  $p+p$  and Au+Au collisions at  $\sqrt{s_{NN}} = 200 \text{ GeV}$ .

## Chapter 6

# Exploring $b$ -jet- $B$ -meson correlations

### 6.1 Introduction

Inspired by [10], in this chapter, we further explore  $b$ -jet- $B$ -meson correlation via the non-prompt- $D$  meson decay product from the  $B$ -meson. The results are still very preliminary, and are intended for internal discussion within the collaboration. Meanwhile, we would like to use this exploration to demonstrate new probes enabled by combining high precision tracking and high rate jet detector at RHIC.

Besides the di- $b$ -jet correlation studies as discussed in the last chapter, measuring the  $b$ -jet- $B$ -meson correlations with the  $B$ -meson within either the leading or the away-side  $b$ -jet can help understand the  $b$ -quark  $\rightarrow B$ -meson fragmentation process and extend the away-side transverse momentum coverage down to  $p_T = 0$ . As this study can tag the partonic kinematics of the  $D$  meson, it would also help understand the origin of non-prompt- $D$  meson, and help the interpretation of the single non-prompt- $D$  meson study as also performed by the HF topical group.

To initiate this exploration, this note currently focuses on studying the  $b$ -jet- $B$ -meson correlations with the away side pairs from the  $B \rightarrow D \rightarrow \pi K$  decay chain in PYTHIA8 truth records, in order to estimate the signal yield. We are working on quantifying the signal purity and efficiency via GEANT4 based simulation to produce a realistic projection on the significance of this measurement. Furthermore, although not discussed in this note, the analysis techniques developed from this study allows the search of prompt- $D$ -meson tagged jets, which will provide the information about  $c$ -jets, formation of Charmed hadrons, and help understand the mass/flavor dependent parton energy loss mechanisms.

## 6.2 Simulation and Analysis Setup

In this first exploration stage, 18M PYTHIA8 Hard QCD simulation events were used to estimate the cross section. Only events contain leading truth  $b$ -jets with  $p_T > 20\text{GeV}/c$  and within  $|\eta| < 1.0$  are used in this analysis. For non-prompt  $D$ -meson reconstruction, we focus on the  $D^0 \rightarrow \pi K$  decay channel. PYTHIA8 truth charged kaons and pions with  $p_T > 0.3\text{GeV}/c$ ,  $|\eta| < 1.0$  and originated from a displaced vertex are used in this study. In addition, charged pions and kaons candidates are required to be within the away-side region of the leading  $b$ -jet ( $|\Delta\phi| > \frac{2}{3}\pi$ ). To form the charge neutral  $D$ -meson candidates, pairs of kaon and pion are required to have opposite charge sign, and the differences between their decay vertex- $z$  component should be within 100 microns. For the preliminary result of this study, we use the truth information recorded in the PYTHIA8 simulation. Kaons and pions should come from the same  $D$ -meson decay and the  $D$ -meson should be the decay product of a  $B$ -meson. Another case included in the analysis sample is that the  $D$ -meson is the decay product of another  $D$ -meson from a  $B$ -meson decay. The luminosity is based on sPHENIX continuous run from 2022 to 2027 projection which results in 240B MB Au+Au collisions without requiring a Au+Au trigger [13]. The physical projection scales the distributions in PYTHIA8 simulation with the  $N_{coll}$  in MB (0-100%) Au+Au collisions and the total projected luminosity.

Since a different PYTHIA8 sample than that in Section 2.2 is used in this  $b$ -jet and non-prompt  $D$ -meson correlations study, a cross-check is done to study the inclusive jet and inclusive  $b$ -jet relative yields. A consistent result is achieved between this study and the early studies as shown in Figure 2.1. For the detector response part, assumption is made about the  $b$ -jet tagging efficiency is 0.5 and its purity is 1, and the  $b$ -jet purity with away-side tagged  $B$ -meson needs further quantification. According to the  $B$ -meson and non-prompt  $D$ -meson studies, the non-prompt  $D$ -meson reconstruction efficiency is assumed as 0.6 and its purity is 1. Further studies will also include a more realistic purity determined from a fast simulation with pre-determined detector resolutions from a full GEANT4 simulation.

## 6.3 Results (Internal discussion use only)

The observable is defined as the ratio of the transverse momentum of the non-prompt  $D$ -meson over the transverse momentum of the leading  $b$ -jet,  $z_j$ . A preliminary projection of the transverse momentum balance of a leading  $b$ -jet and a away-side non-prompt  $D$ -meson correlations in 240B MB Au+Au collisions is shown in Figure 6.1.

With the same luminosity of 200 GeV Au+Au collisions, the preliminary result of the azimuthal correlations between a leading  $b$ -jet and a away-side  $B$ -meson is shown in the left panel of Figure 6.2 and the correlations between a leading  $b$ -jet and a away-side non-prompt  $D$ -meson is shown in Figure 6.2.

Since the purity for the  $b$ -jet and  $B$ -meson are assumed to be 100%, these



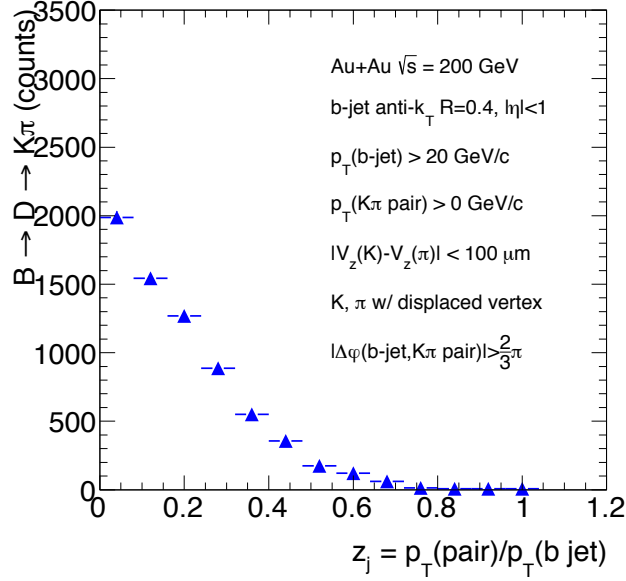


Figure 6.1: For internal discussion only: preliminary projection of transverse momentum balance of  $b$ -jet and non-prompt  $D$ -meson correlations in 240B MB Au+Au collisions (0-100% centrality) at  $\sqrt{s_{NN}} = 200$  GeV. A  $R_{AA}$  of 0.6 is assumed without a  $p_T$  dependence. As purity is still under study, this projection assumed 100% purity for both  $D$ -meson and  $b$ -jet. Therefore, it gives the upper limit of the statistical significance.

610 preliminary results only represent the max statistics significance we could obtain.  
 611 Therefore, Figure 6.1 and 6.2 are not to be used in external showing, while the  
 612 purity quantification via simulation is being performed.

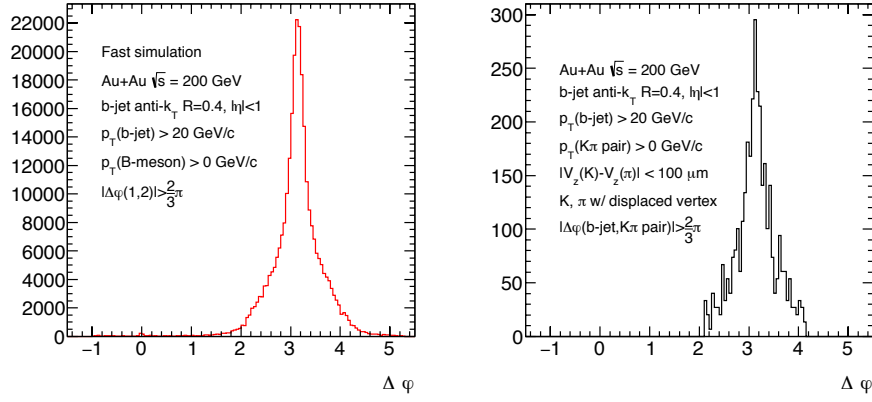


Figure 6.2: For internal discussion only: preliminary projection of azimuthal correlations between a leading  $b$ -jet and a away-side  $B$ -meson (left) or non-prompt- $D \rightarrow \pi K$  (right) in 240B MB (0-100% centrality) Au+Au collisions at  $\sqrt{s_{NN}} = 200$  GeV. The  $B$ -meson channel is not measured, but represent the source distribution for the non-prompt- $D$  observables. Note, the  $B$ -meson channel has much higher statistics as the non-prompt- $D \rightarrow \pi K$ , as the later case suffer from the branching ratio of the decay chain. As purity is still under study, this projection assumed 100% purity for both  $D$ -meson and  $b$ -jet. Therefore, it gives the upper limit of the statistical significance.

## 613 Chapter 7

## 614 Final words

615 This note is a snapshot of the HF-jet studies performed by the HF topical group.  
616 We demonstrated the capability of tagging  $b$ -jet using the sPHENIX with MVTX  
617 upgrade in  $p+p$  and central Au+Au environment using GEANT4 simulation  
618 and reconstruction. MVTX upgrade is critical in enabling the  $b$ -jet capability.  
619 Then projection for  $b$ -jet nuclear modification and di- $b$ -jet correlation are pre-  
620 sented. In the end, the progress of exploring the  $b$ -jet- $B$ -meson correlations is  
621 discussed.

622 Work are on-going to update these studies with the in-development new  
623 tracking software and improving the purity studies via simulation. Many more  
624 topics are also open for volunteers, as discussed in the [Heavy Flavor Topical](#)  
625 [Group Wiki](#)

# Bibliography

- [1] The RAVE/VERTIGO vertex reconstruction toolkit and framework. [3.2](#)
- [2] A. Adare et al. An Upgrade Proposal from the PHENIX Collaboration. 2015. [1.1](#), [1.4](#), [3.1](#), [5.1](#)
- [3] A. Adare et al. Centrality-dependent modification of jet-production rates in deuteron-gold collisions at  $\sqrt{s_{NN}}=200$  GeV. *Phys. Rev. Lett.*, 116(12):122301, 2016. [2.2](#), [2.1](#)
- [4] Matteo Cacciari, Stefano Frixione, and Paolo Nason. The p(T) spectrum in heavy flavor photoproduction. *JHEP*, 03:006, 2001. [2.2](#), [2.1](#)
- [5] Matteo Cacciari, Mario Greco, and Paolo Nason. The P(T) spectrum in heavy flavor hadroproduction. *JHEP*, 05:007, 1998. [2.2](#), [2.1](#)
- [6] Serguei Chatrchyan et al. Evidence of b-Jet Quenching in PbPb Collisions at  $\sqrt{s_{NN}} = 2.76$  TeV. *Phys. Rev. Lett.*, 113(13):132301, 2014. [Erratum: *Phys. Rev. Lett.* 115, no. 2, 029903 (2015)]. [1.1](#), [1.4](#), [1.4](#), [3.3.2](#), [3.6](#), [4.3](#)
- [7] CMS Collaboration. Splitting function in pp and PbPb collisions at 5.02 TeV. 2016. [1.4](#)
- [8] CMS Collaboration. Transverse momentum balance of b-jet pairs in PbPb collisions at 5 TeV. 2016. [1.1](#), [1.4](#), [1.4](#), [3.3.2](#), [4.3](#), [5.3](#)
- [9] Jinrui Huang, Zhong-Bo Kang, and Ivan Vitev. Inclusive b-jet production in heavy ion collisions at the LHC. *Phys. Lett.*, B726:251–256, 2013. [1.1](#), [1.4](#), [2.1](#), [2.3](#), [2.2](#), [5.1](#)
- [10] Jinrui Huang, Zhong-Bo Kang, Ivan Vitev, and Hongxi Xing. Photon-tagged and B-meson-tagged b-jet production at the LHC. *Phys. Lett.*, B750:287–293, 2015. [1.4](#), [6.1](#)
- [11] K Kauder. Measurement of the Shared Momentum Fraction  $z_g$  using Jet Reconstruction in p+p and Au+Au Collisions with STAR. 2016. [1.4](#)
- [12] Andrew J. Larkoski, Simone Marzani, Gregory Soyez, and Jesse Thaler. Soft Drop. *JHEP*, 05:146, 2014. [1.4](#)

- 654 [13] Jamie Nagle and Dennis Perepelitsa. sphenix ve-year (2022-2026) running  
655 scenario and luminosity projections. 2017. [1.3](#), [6.2](#)
- 656 [14] E. Norrbin and T. Sjostrand. Production and hadronization of heavy quarks.  
657 *Eur. Phys. J.*, C17:137–161, 2000. [1.4](#), [5.1](#)